Advanced Energy Materials

ADVANCED ENERGY MATERIALS
www.advenergymat.de

RESEARCH ARTICLE OPEN ACCESS

Synergistic Optimization of Cathode Composite Architecture and Stack Pressure for High-Performance All-Solid-State Chloride-Ion Batteries

Soutam Panja[1,2] | Anantha Padmanabhan Gopikuttan[1,2] | Manuel Mundszinger[3] | Amr Radwan[1,2] | Hong Chen[4] | Johannes Biskupek[3] | Oliver Clemens[5] | Maximilian Fichtner[1,2,6]

[1]Helmholtz Institute Ulm for Electrochemical Energy Storage (HIU), Ulm, Germany | [2]CELEST Green Energy Lab Ulm, Ulm University, Ulm, Germany | [3]Electron Microscopy Group of Material Science, Ulm University, Ulm, Germany | [4]Lehrstuhl für Anorganische Chemie mit Schwerpunkt Neue Materialien, TUM School of Natural Sciences – Department Chemie, Technische Universität München, Garching, Germany | [5]Institute for Materials Science, Materials Synthesis Group, Stuttgart University, Stuttgart, Germany | [6]Institute of Nanotechnology, Karlsruhe Institute of Technology (KIT), Karlsruhe, Germany

Correspondence: Soutam Panja (soutam.panja@kit.edu) | Maximilian Fichtner (m.fichtner@kit.edu)

Received: 20 February 2026 | **Revised:** 26 June 2026 | **Accepted:** 6 July 2026

Keywords: chloride-ion batteries | composite cathode | perovskites | solid-state batteries | VOCl

ABSTRACT

Chloride-ion batteries (CIBs) represent a promising post-lithium energy storage platform combining high theoretical energy density with elemental sustainability. However, All-Solid-State CIBs (ASS-CIBs) remain hindered by limited ionic transport and interfacial instability. Here, we demonstrate a high-performance VOCl/$CsSn_{0.9}In_{0.067}Cl_3$ (CSIC)/In system wherein systematic optimization of the cathode composite identifies an optimal 30:60:10 (VOCl/CSIC/C) ratio, delivering an initial specific capacity of 169 mAh g^{-1}. X-ray diffraction (XRD) with Rietveld refinement and field-emission scanning electron microscopy (FESEM) confirmed phase purity and uniform particle distribution, while increasing stack pressure from 130 to 400 MPa markedly enhanced interfacial contact and active material utilization. The optimized configuration sustained stable cycling over 500 cycles at 0.1 mA cm^{-2} with nearly 100% Coulombic efficiency. Time-resolved electrochemical impedance spectroscopy (EIS), analyzed using the distribution of relaxation times (DRT) method, identified the VOCl–CSIC cathode interface as the dominant resistance contributor, while the In–CSIC anode remained comparatively stable. Ex situ XRD and focused ion beam–scanning electron microscopy (FIB-SEM) corroborated these findings, revealing reversible phase transitions alongside structural breathing, particle cracking, and void formation. This work provides a kinetically and structurally rationalized design strategy toward durable ASS-anionic shuttle batteries based on powdered electrode architectures.

1 | Introduction

The widespread adoption of lithium-ion batteries has been pivotal in powering portable electronics, electric vehicles, and stationary energy storage. Nevertheless, concerns regarding the limited availability of lithium resources, rising material costs, and the ongoing risk of thermal runaway due to flammable liquid electrolytes have driven the pursuit of post-lithium battery technologies to diversify the material basis and to further drive economic viability [1, 2]. Among the different alternatives, batteries based on multivalent cations and anion shuttle mechanisms have garnered significant attention for their potential

Soutam Panja and Anantha Padmanabhan Gopikuttan contributed equally to this work.

to deliver high energy density using earth-abundant materials [3–8].

Anion shuttle batteries, in particular, leverage the reversible transport of anions such as chloride, enabling multi-electron transfer processes and mitigating dendrite formation [9, 6]. CIBs have emerged as a compelling class within this family, offering high volumetric energy density, low cost, and the use of non-critical elements. Early CIB development initially focused on ionic liquid electrolytes, which, despite their non-volatility and wide electrochemical windows, suffered from sluggish chloride-ion transport kinetics [10]. Subsequent efforts with conventional liquid electrolytes improved ionic conductivity but introduced new challenges, including active material dissolution, interfacial instability, and limited cycle life, all of which have restricted the practical deployment of CIBs [11, 12].

Transitioning from liquid to ASS-CIBs effectively overcomes challenges like active material dissolution, while significantly enhancing chemical stability. This progress has been pivotal in advancing safer, more robust CIB technologies [13, 14]. Nevertheless, the realization of high-performance ASS-CIBs introduces new challenges, particularly in achieving optimal solid–solid interfacial contact and percolation networks for both ionic and electronic transport within composite electrodes [15]. The architecture of the composite cathode, specifically the distribution and connectivity of active material, solid electrolyte, and conductive carbon, emerges as a decisive factor in governing rate capability, energy density, and long-term cycling stability [13, 14, 16]. Operational parameters such as stack pressure, temperature, and current density further influence electrode densification, contact quality, and overall electrochemical response [17–19].

Among the emerging cathode families for CIBs, metal oxychlorides have garnered growing attention for their unique structural robustness and redox adaptability. The incorporation of oxygen into the metal chloride lattice enhances framework stability through strong Lewis acid–base interactions with metal centers, which effectively mitigates metal ion dissolution in cells with liquid electrolytes, a persistent issue in pure chloride cathodes. This structural reinforcement not only stabilizes the lattice during repeated conversion reactions but also helps preserve electrode integrity, leading to improved cycling reversibility and capacity retention. Owing to their dual anionic composition and tunable electronic configurations, metal oxychlorides (e.g., FeOCl, BiOCl, etc.) exhibit versatile redox activity and favourable diffusion kinetics, making them promising candidates for next-generation solid-state CIBs as well as related systems such as sodium-ion batteries (NIBs) [20, 12, 21].

VOCl, a representative member of this class, was first reported as a cathode material for chloride-ion batteries over a decade ago [22], with an electronic conductivity of approximately 2×10^{-8} Scm^{-1} at room temperature, derived from earlier electrical resistivity measurements on single crystalline VOCl [23]. Its layered structure, robust framework, and the presence of these strongly bound, Lewis basic oxygen atoms effectively mitigate the dissolution problems that plague many metal chloride cathodes. The electrochemical mechanism of VOCl is well established with lithium as an anode for CIB systems and is described by the conversion reaction, accompanied by solvent intercalation into the layered material:

$$VOCl + Li + PP_{14}Cl - PC \rightarrow VO * PP_{14}Cl - PC + LiCl \quad (1)$$

where VOCl serves as the cathode and lithium metal as the anode. The robustness of the VOCl host structure resists dissolution via the stabilization of solvent intercalation and enables more stable cycling, making it a promising candidate for solid-state chloride-ion systems. However, the translation of this chemistry to chloride-ion configurations other than Li anodes, particularly in ASS architectures lacking solvents, remains largely unexplored.

The selection of suitable anode materials is also a critical factor in the design of chloride-ion battery architectures. Indium metal has been proposed as a candidate anode material in preliminary studies of chloride-ion systems due to its theoretical redox activity [24]. In this work, we introduce a powdered indium anode composite paired with a $CsSn_{0.9}In_{0.067}Cl_3$ (CSIC) solid electrolyte, a configuration not previously explored in solid-state CIBs to our knowledge.

Notably, CSIC exhibits high chloride-ion conductivity (σ_{ion} = 3.45×10^{-4} S cm^{-1} at 25°C) and remarkably a low electronic conductivity (σ_{elec} = 3.7×10^{-11} S cm^{-1} at 1 V under DC polarization), making it an ideal solid electrolyte for efficient ion transport while suppressing electronic leakage [25]. While a detailed electrochemical assessment of the anode–electrolyte interface, particularly its stability under polarization, remains an avenue for future investigation, ex situ XRD analyses of cycled electrodes unveiled discernible phase conversion processes along with minor electrolyte degradation. These observations highlight the dynamic structural evolution that occurs during repeated cycling. Advancing the interfacial stability of indium-based systems will require targeted optimization of electrode architecture and implementation of interfacial engineering strategies to suppress degradation while enabling sustained ion transport.

A systematic investigation was undertaken through the careful preparation of VOCl-based composite cathodes. Four distinct formulations with varying ratios of VOCl, CSIC, and carbon were prepared to optimize ionic and electronic percolation. The influence of stack pressure (≈ 130, ≈ 250, and ≈ 400 MPa), current density, and temperature on cell performance was evaluated. FIB cross-sectional imaging and Rietveld-refined XRD were further used to correlate electrochemical performance with electrode morphology. FIB-SEM provided critical insights into interfacial contact evolution, particle cracking, and void formation, while XRD confirmed the structural integrity of the solid electrolyte post-cycling [26, 27].

Although ASS-CIBS offer a promising anionic electrochemistry, their practical realization faces a profound physical and engineering challenges at the electrode-electrolyte interface. Our current understanding of these microstructural challenges stems from extensive development of all-solid-state lithium batteries (ASS-LIBs). Optimization of the cathode active material (CAM), solid electrolyte (SE), and conductive carbon (C) ratio is universally recognized as a critical strategy to establish robust ionic and

electronic percolation networks in ASS-LIBs. For example, in sulfide and halide-based electrolyte systems, balancing CAM:SE ratio and managing carbon distribution have been shown to be essential for achieving high active-material utilization while mitigating interfacial resistance and diffusive limitations [28–30]. Furthermore, the application of stack pressure has proven to be a critical parameter across all solid-state battery classes as they cannot naturally adapt to volume expansion and contraction ("breathing") of the active materials during cycling. Recent studies have demonstrated that identifying the optimum stack pressure, typically falling within the 5–75 MPa range for brittle sulfide and halide systems, is a delicate balancing act. Insufficient pressure leads to high interfacial impedance and void formation, while excessive pressure can crack particles and mechanically degrade the composite cathode structure [31–33]. Despite these well-established principles in ASS-LIBs, analogies systematic studies regarding composite cathode formulation and stack pressure regulation in ASS-CIBs, particularly using oxychloride cathode and CSIC electrolytes, remain remarkably scarce.

Beyond these challenges in composite architecture and pressure engineering, a quantitative understanding of how interfacial resistance evolves during operation in the VOCl/CSIC/In system is equally lacking. Although electrochemical impedance spectroscopy (EIS) is widely used in solid-state battery research, conventional Nyquist analysis of composite powder electrodes suffers from the overlap of multiple relaxation processes, making the unambiguous assignment of cathode, anode, and electrolyte contributions inherently difficult. The distribution of relaxation times (DRT) method addresses this by converting impedance data into a time-domain representation, allowing individual polarization processes to be resolved without assuming an equivalent circuit model. DRT has been successfully applied in sulfide and halide-based all-solid-state lithium battery systems to track interfacial resistance growth and identify dominant kinetic bottlenecks during cycling [34–36]. Yet, its application to chloride-ion systems remains unexplored. In this work, time-resolved EIS and DRT analysis are therefore performed on symmetric VOCl/CSIC/VOCl and In/CSIC/In cells as well as on the full VOCl/CSIC/In cell, enabling electrode-resolved impedance tracking that directly connects to the microstructural and phase evolution characterized by FIB-SEM and ex situ XRD.

To provide a comprehensive overview of the experimental strategy and key governing factors explored in this work, Figure 1 illustrates the architecture of the ASS-CIB system, the systematic workflow for cathode composite optimization, and the critical role of stack pressure in determining electrode compactness and interfacial contact. As illustrated, a range of cathode composite ratios, abbreviated as CAM 1 (55:15:30), CAM 2 (45:25:30), CAM 3 (30:60:10), and CAM 4 (20:50:30), were systematically investigated, and stack pressure influence was studied to elucidate their influence on microstructure and electrochemical performance. The schematic further highlights how lower stack pressures result in reduced compactness and increased interparticle gaps, underscoring the importance of mechanical engineering in achieving high-performance solid-state batteries. This integrated approach establishes the framework for the detailed experimental results and mechanistic insights presented in the following sections [37, 38].

2 | Results and Discussions

2.1 | Uniform Distribution and Phase Stability in Cathode Composites

Figure 2a presents the XRD data and corresponding Rietveld refinement of the 30:60:10 (CAM 3) cathode composite, with analogous refinements for CAM 1, 2, and 4, as well as pristine VOCl powder (Figure S1a) and CSIC (Figure S1b), provided in Figure S1c,d,e. The refinement profiles confirmed that the ball-milling process with lower rotational speed preserved the crystal structure of all components across all composite ratios, as evidenced by the absence of peak shifts or new reflections indicative of side reactions. The refined lattice parameters of VOCl and CSIC, summarized in Table S1, remain within experimental uncertainty across all samples, underscoring the robust structural stability of both the active material and electrolyte throughout the processing steps.

Figure 2b represents SEM micrographs of VOCl pristine particles, while Figure 2c,d depicts the prepared cathode composite pellets of CAM 3. Additional images for CAM 1, 2, and 4 are provided in Figure S2. As depicted in Figure 2b, the pristine VOCl particles exhibited a distinct, elongated, flat, rice grain-shaped morphology. Laser diffraction particle size analysis further quantified the powder as having D_{10} = 2.04 μm, D_{50} = 6.32 μm, and D_{90} = 14.1 μm (Figure S11), confirming that the VOCl particles span a broad size distribution within the micrometer range. The distributions of active particles within the cathode composite are illustrated in Figure 2c, as further illustrated by FIB-SEM cross-sections discussed in Section 2.3 (Figure 4b). These observations have significant implications for particle packing and interfacial contact within the composite. The dark-colored particles in Figure 2d represent the VOCl active materials.

The ball milling mixing method resulted in minimal cleavage of the active materials, as illustrated in Figure 2c. The composition and concentration of the electrolyte affect the conductivity of halide ions within the bulk of the composite, as the active material has limited ionic and electronic conductivity [38]. Therefore, a uniform distribution of CAM and substantial contact with the electrolyte significantly affect the performance. Subsequently, SEM-EDS analysis was conducted (Figure 2d) to confirm the distribution of the cathode, electrolyte, and carbon. The elemental distribution of vanadium (yellow), cesium (red), and carbon (purple) was selected to provide a comprehensive overview of CAM, SE, and conductive carbon within the composite (Figure 2). Due to VOCl being a poor electronic conductor, achieving a fine distribution of active materials with SE and conductive carbon is essential for improved electrochemical performance [39]. According to percolation theory, the electrochemical performance is significantly influenced by the fine distribution of particles and the particle size distribution of active materials and SE [15].

Since reducing particle sizes is known to minimize ionic transport resistance and maximize solid-solid contact across the electrode-electrolyte interface, thereby leading to better distribution of the active material within the cathode composite [40], a subsequent approach involving ball-milling at a higher rotational speed was

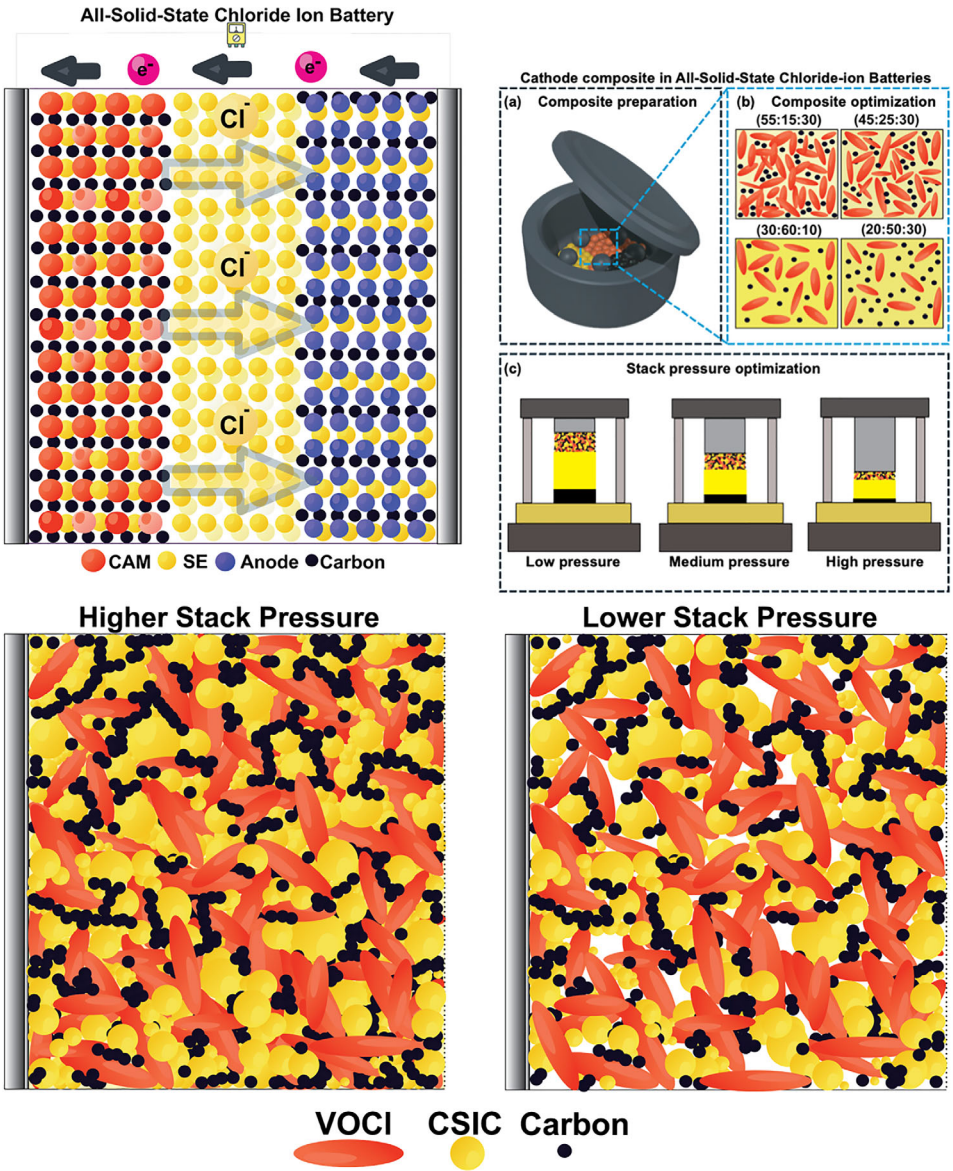

FIGURE 1 | Schematic and workflow for VOCl/CSIC/In ASS-CIB cell assembly and microstructural control. (a) Schematic illustration of the VOCl/CSIC/In full cell architecture. (b) Stepwise workflow for cathode composite preparation, composite ratio optimization, and pressure application. (c) Microstructure of the cathode composite under high stack pressure, highlighting densely packed VOCl, C, and CSIC particles. (d) Microstructure under low stack pressure, illustrating a loosely packed cathode composite.

explored. While this method achieved particles in the broad size range of 100 nm–5 μm (Figure S9a,b), the high-speed processing still successfully produced and distributed the reduced cathode particles within the composite (Figure S9c), with the accompanying EDS elemental mapping confirming the uniform distribution of V, Cs, Cl, and C. However, the increased mechanical energy and highly reduced particle dimensions led to detrimental structural changes [41]. The XRD analysis (Figure S8) of these size-reduced particles clearly indicated amorphization and increased reactivity, ultimately resulting in the formation of minor V_2O_3 (COD database code: 2106583) phase. This demonstrates a critical trade-off, where aggressive size reduction compromises the structural integrity of the active material despite achieving the desired particle morphology and uniform composite distribution.

2.2 | Electrochemical Performance Under Variable Operating Conditions

To ensure optimal cell performance and reproducibility, all electrochemical measurements in this study were conducted at 60°C. This temperature was selected based on the significant increase in chloride-ion conductivity of the CSIC solid electrolyte at elevated temperatures, as determined by electrochemical impedance spectroscopy (EIS). Specifically, the ionic conductivity rises from 3.45×10^{-4} S cm^{-1} at 25°C to 6.9×10^{-4} S cm^{-1} at 60°C, as evidenced by the comparative Nyquist plots shown in Figure S4. The enhanced ionic conductivity at 60°C enables more efficient chloride-ion transport, thereby supporting consistent and reliable electrochemical performance throughout this study.

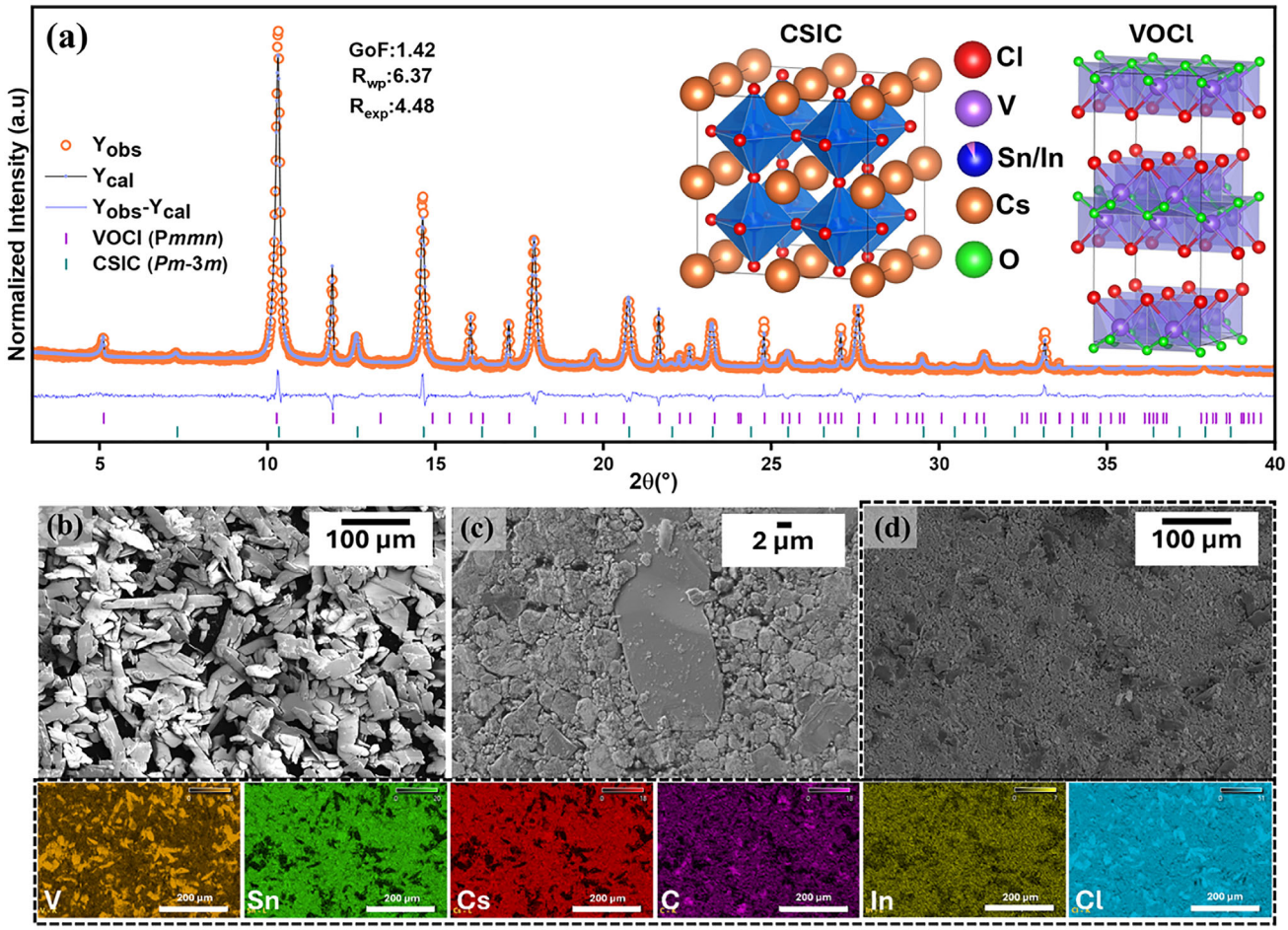

FIGURE 2 | (a) Rietveld refinement of the powder XRD pattern for the CAM 4 cathode composite, with crystal structures of CSIC and VOCl shown as insets. (b) SEM image of synthesized VOCl particles. (c) High-magnification SEM image of the CAM 3 cathode composite. (d) SEM image of the CAM 3 pellet with EDS elemental maps for V, Sn, Cs, C, In, and Cl, respectively (bottom panels left to right).

Figure 3 presents a comprehensive analysis of the electrochemical behaviour of CAM composites. Cyclic voltammetry (CV) was employed to probe the redox mechanisms of the optimized cathode composite. Figure 3a shows the CV profile of the CAM 3 composite over a potential window of −1.0 to 1.0 V vs. In at a scan rate of 0.05 mV s^{-1}. In the first cathodic scan, a broad reduction feature spanning 0 to −0.5 V is observed, which is plausibly associated with the conversion of VOCl to a reduced state via chloride ion extraction [24]. The corresponding anodic scan displays a prominent oxidation peak between 0.1 and 0.6 V vs. In, which can be reasonably attributed to the reverse process, involving chloride ion re-insertion and re-oxidation of vanadium. While this interpretation aligns with the expected redox chemistry of VOCl systems, the precise mechanistic details may involve additional complexities.

The reversible nature of these redox processes, evidenced by the similar potential ranges for reduction and oxidation across multiple cycles, is characteristic of quasi-reversible behaviour in cyclic voltammetry [42, 43]. This is further supported by the progressive decrease in peak current density and increased peak broadening observed with continued cycling. Such quasi-reversible features may arise from kinetic limitations associated with solid–electrolyte interface evolution or a gradual loss of electrochemically active material, both of which could contribute to the observed capacity fading during extended operation. Notably, both cathodic and anodic scans exhibit shoulder features particularly evident at ∼0.5 V during oxidation, pointing to a multi-step reaction mechanism that may involve intermediate phases or structural relaxation of the VOCl host during conversion [22].

The emergence of subsidiary shoulder peaks aligns with the complex conversion chemistry inherent to metal oxychlorides and may reflect subtle interfacial phenomena involving the CSIC electrolyte during redox cycling, further explored in Section 2.3. These features provide electrochemical evidence for additional redox activity beyond the primary VOCl/VO transformation. While the precise nature of these processes remains to be fully characterized, the shoulder peaks likely correspond to intermediate phases formed through multi-step redox pathways, as observed in previous studies with Mg anodes [22]. These CV insights underpin the capacity evolution and cycling behaviour observed in galvanostatic testing, underscoring the need for further investigation into the multi-phase redox mechanisms in this system.

These redox features are mirrored in the galvanostatic charge–discharge profiles (Figure 3b,c), where pronounced voltage

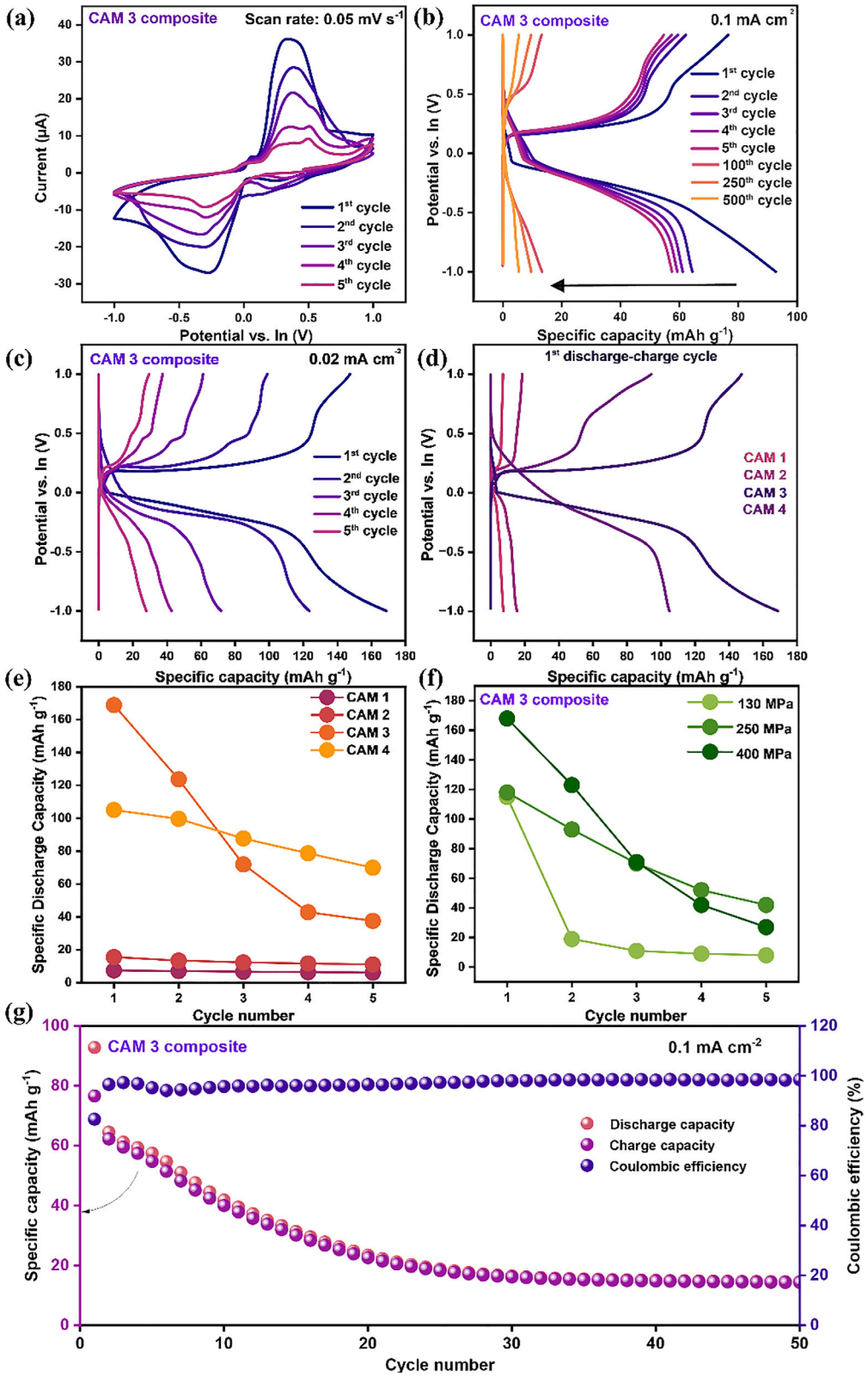

FIGURE 3 | (a) CV curve of CAM 3 composite. (b) Charge–discharge profiles of CAM 3 at 0.1 mA cm^{-2} for selected cycles. (c) Charge–discharge profiles of CAM 1 at 0.02 mA cm^{-2} for the first five cycles. (d) Comparison of first discharge–charge cycles for CAM 1–4 composites. (e) Comparison of discharge capacity vs. cycle number for composites with varying component ratios. (f) Comparison of discharge capacity vs. cycle number for CAM 3 pressed at 130, 250, and 400 MPa. (g) Long-term cycling performance of CAM 3 at 0.1 mA cm^{-2}.

plateaus are observed near −0.1 V vs. In during discharge and between 0.1 and 0.3 V during charge vs. In. These plateaus are indicative of phase transformations between VOCl and reduced vanadium oxide species ($VOCl_{1-x}/VO_x$), and their correspondence with the CV peaks underscores the reversibility of the underlying electrochemical reactions [44, 22].

A notable aspect of the charge–discharge profiles is the intersection point of the charge and discharge curves, which consistently occurs at approximately 0.1 V vs. In across all composite formulations. This point, often referred to as the voltage plateau midpoint or average cell potential, marks the voltage at which the chemical potentials of the oxidized and reduced phases are equal during the (de)chlorination reaction. The discharge and charge curves crossover at the same potential over the other composite ratios, suggesting that the redox chemistry is governed primarily by the intrinsic thermodynamics of the $VOCl/VOCl_{1-x}$ system, rather than by variations in electrode composition or architecture. Such a well-defined equilibrium potential is characteristic of a two-phase reaction mechanism, as commonly observed in systems with reversible conversion [45] or intercalation processes [46, 47].

The comparative first discharge–charge cycles for CAM 1–4 composites (Figure 3d) reveal that the CAM 3 composite delivered the highest initial discharge capacity of 169 mAh g^{-1}. This value corresponds to 64% of the theoretical capacity (261 mAh g^{-1}) and reflects the transfer of approximately 0.7 electrons per VOCl formula unit. Among the four compositions, CAM 3 exhibited superior performance due to an optimized balance between ionic and electronic conductivity, underscoring the critical role of compositional tuning. Although CAM 4 showed comparatively stable retention, its lower active material loading (20 wt.%) and higher carbon content (30 wt.%) resulted in a lower initial capacity and may limit direct ionic access to VOCl surface sites, making CAM 3 the more effective formulation in terms of total delivered capacity and active material utilization. The cycling data in Figure 3e further support this trend, where the CAM 3 composite consistently demonstrated superior capacity retention and stability compared to other formulations.

The effect of densification with stack pressure is explored in Figure 3f, where increasing the stack pressure from 130 to 400 MPa results in a marked improvement in initial specific capacity, rising from 115 to 169 mAh g^{-1}. In order to mitigate the risk of short circuits and enhance mechanical stability, an electrolyte mass of 80 mg was introduced. The enhanced interfacial contact between the composite components at higher pressures is believed to reduce charge transfer resistance and promote more efficient ion and electron transport. However, at elevated current densities, kinetic limitations become increasingly significant, likely due to solid-state diffusion constraints and the relatively large VOCl particle size, which can hinder chloride ion mobility [48].

Long-term cycling performance is shown in Figure 3g, which demonstrates that the optimized CAM 3 composite maintained stable discharge and charge capacities with a coulombic efficiency close to 100% over 500 cycles. These results highlight the strong cyclability and reversibility of the chloride ion storage mechanism in the optimized composite. The prolonged cycling stability curve till 500 cycles in Figure S7 reveals that even though sharp capacity fading was observed in the initial 30 cycles, the system demonstrated notable persistence; it retained almost 79% capacity between 100 and 250 cycles, and while retention slightly lowered to approximately 55% between 250 and 500 cycles, the composite still continued to cycle. To further optimize this behavior and address these constraints, we investigated various scenarios, including the reduction of particle size via high-speed ball milling. However, this approach proved detrimental; even when utilizing the optimized CAM 3 (30:60:10) composite ratio and higher stack pressures, the resulting composite (morphology detailed in Figure S9c) exhibited significantly compromised electrochemical performance, characterized by low capacities (Figure S10). This failure conclusively demonstrates that mechanical over-crushing induces irreversible structural damage, thereby highlighting the necessity of pursuing a direct synthesis approach for controlled, small particle morphology to achieve sustainable improvements in electrochemical kinetics and stability. Collectively, these findings emphasized the critical interplay between electrode composition, processing conditions, particle size, and electrochemical performance in developing high-capacity, stable CIBs. In contrast to many all-solid-state batteries that use dense metal foils as at least one electrode, our VOCl/CSIC/In cell employed powder-based composite electrodes on both sides; when such cells are pre-pressed at 400 MPa and then operated at ≈ 65 MPa (Figure S13), the capacity is clearly reduced, indicating that this lower stack pressure is insufficient to maintain the required consolidation and solid–solid contact in the powder architecture. The impact of these interfacial changes on the cell resistance is discussed in Section 2.4, where time-resolved EIS and DRT analysis on symmetric and full cells are used to isolate and quantify the individual contributions.

2.3 | Cycling-Induced Degradation and Phase Evolution

To elucidate the influence of stack pressure on the internal microstructure and phase evolution of the CAM 3 cathode composite, cross-sectional FIB-SEM imaging was performed on samples subjected to different stack pressures both before and after electrochemical cycling (Figure 4a–c). In the pristine state, the FIB-SEM cross-section of the composite pressed at 250 MPa (Figure 4a) reveals a non-uniform spatial arrangement of the active material, solid electrolyte, and conductive carbon, with noticeable regions of insufficient interfacial contact. Increasing the stack pressure to 400 MPa (Figure 4b) resulted in a substantially compact composite architecture, characterized by enhanced connectivity and more continuous contact between the CAM and SE/C phases. Despite this densification, localized bending and deformation of the VOCl particles are observed, indicating that mechanical stress under compression is accommodated by particle flexure rather than by the complete elimination of inter-particle voids. These observations underscore the critical role of stack pressure in optimizing electrode architecture and suggest that further reductions in particle size and improvements in size uniformity could facilitate even more effective densification and interfacial contact [37].

After 100 electrochemical cycles, FIB-SEM analysis of the cathode composite pressed at 250 MPa stack pressure (Figure 4c)

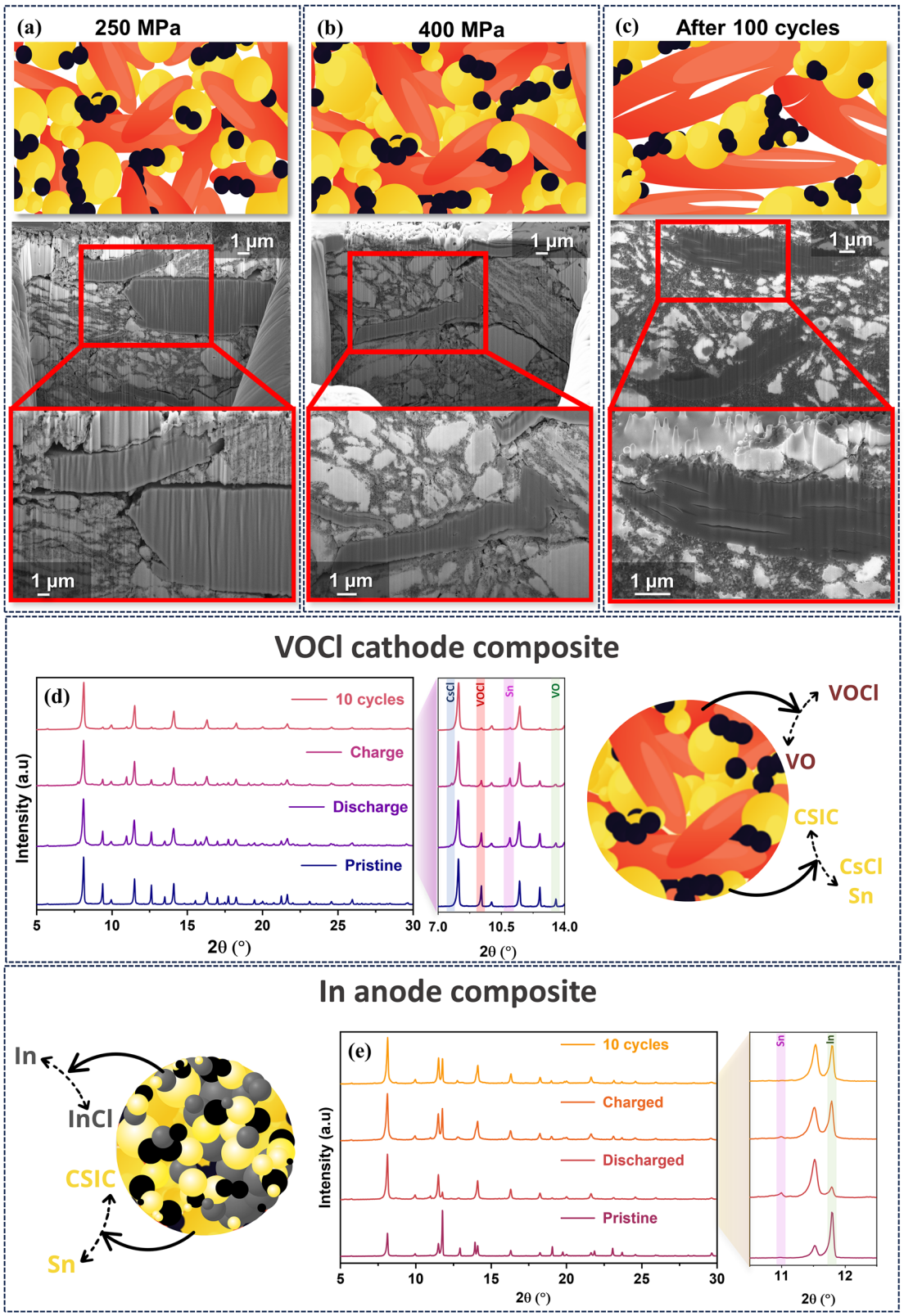

FIGURE 4 | (a–c) Schematic illustrations and FIB-SEM cross-sectional images of the cathode composite pressed at (a) 250 MPa, (b) 400 MPa, and (c) after 100 cycles. (d,e) XRD patterns of pristine, discharged, charged, and after 10 cycles for composite electrodes: (d) VOCl and (e) indium.

reveals significant microstructural evolution. The CAM particles displayed pronounced exfoliation and "breathing," with the formation of internal cracks and voids throughout the bulk. These features are consistent with repeated chloride ion extraction and insertion, which induce considerable volume changes and lattice relaxation within the layered VOCl structure [40]. The development of internal voids and the disruption of percolation pathways likely impede both ionic and electronic transport, providing a mechanistic basis for the observed capacity fading during cycling [26]. In addition to the qualitative FIB-SEM observations, a semi-quantitative pore-segmentation analysis of representative cross-sections after 100 cycles (Figure S14) yields an internal pore area fraction of ≈ 0.2 % within the VOCl/CSIC/C composite, consistent with localized intragranular cracking and interparticle gaps while the bulk of the composite remains largely intact. The relatively large particle dimensions of VOCl, as established by FESEM and laser diffraction (Section 2.1, Figure 2b, and Figure S11), likely contributed to these effects, as particles of such dimensions are generally more susceptible to stress accumulation and intragranular fracture under cycling-induced strain, a phenomenon well-documented in layered oxide cathode materials where larger particle sizes correlate with more pronounced mechanical degradation during electrochemical operation [49]. This indicates that employing controlled particle architectures and enhancing structural uniformity may help mitigate mechanical failures, highlighting the need for systematic investigation in future studies [48]. Post-cycling FIB-SEM characterization was conducted at 250 MPa; however, the higher stack pressure used in the pristine 400 MPa sample likely promoted greater densification and improved initial interfacial contact, which may accounted for the observed superior electrochemical performance.

These effects are expected to enhance the mechanical stabilization of the electrode during cycling and mitigate some microstructural degradation, although certain damage mechanisms may persist. Supplementary images in Figure S3 further illustrate post-cycling particle surface morphology, including the degree of surface cracking and other morphological changes. The cumulative insights from these microstructural and morphological analyses underscore the critical need for optimizing stack pressure, particle dimensions, and electrode architecture. This optimization is essential to enhance interfacial contact, reduce mechanical degradation, and ensure durable cycling stability in solid-state chloride ion systems [38].

To gain deeper insight into the phase evolution accompanying these microstructural transformations, detailed ex situ Rietveld-refined XRD analyses were carried out on both discharged cathode and anode composites (see Figure S6a–d). The overall comparative XRD sequence of cathode composite (Figure 4d) illustrates a gradual amorphization of the VOCl phase with increasing cycle numbers, indicative of structural disordering, a phenomenon also reported in $Fe_{0.5}TiOPO_4$ [50]and SnO_2 [51] electrodes during cycling, as well as in chloride-ion cathodes such as BiOCl [12] and FeOCl [52]. The VOCl phase demonstrated a reduction in phase fraction accompanied by emerging reflections that likely correspond to reduced Vanadium Oxide (VO) (ICSD Collection Code: 60486), included in the refinement (Figure S6b–d). Due to significant overlap in peak positions between VO and VOCl, unambiguous phase differentiation remains challenging. However, the irreversibility of the VOCl transformation process is also well aligned with the partial decomposition of the electrolyte to metallic Sn, as indicated in the following paragraphs.

Detailed analysis reveals that the electrolyte predominantly retained its crystallinity throughout cycling (Figure 4d,e); however, minor degradation is observed, presumably localized at interfacial regions. This degradation is characterized by the emergence of secondary phases—namely Sn (ICSD Collection Code: 106072) and CsCl (ICSD Collection Code: 9008789)—predominantly within the cathode composite (Figure 4d), while Sn is the main impurity detected in the anode composite (Figure 4e and Figure S6f–h). Rigorous Rietveld refinements conducted on ex situ samples from cathode-electrolyte (Figure S6b–d) and anode-electrolyte interfaces (Figure S6f–h) support this targeted localization. These findings suggest that electrolyte degradation primarily occurs within or near interfacial boundaries, whereas the bulk electrolyte maintains its structural integrity over extended cycling, as further corroborated by Rietveld refinement of the CSIC electrolyte after 10 cycles (Figure S5). This indicates that the overall redox mechanism of the VOCl–CSIC–In cell involves coupled cathode and interfacial processes, with at least partly VOCl conversion to a $VOCl_{1-x}$-type (VO-related, most plausibly partly amorphous) phase at the cathode, InCl formation at the anode, and minor electrolyte participation reflected by the emergence of Sn and CsCl [53].

To place the phase evolution and reduction in VOCl reflection intensity in an electrochemical context, cell reactions for the VOCl/CSIC/In system could in part be explained by:

Cathode:

$$\mathrm{VOCl} + x\,\mathrm{e}^- \leftrightarrow \mathrm{VOCl}_{1-x} + x\,\mathrm{Cl}^-$$

Anode:

$$\mathrm{In} + \mathrm{Cl}^- \leftrightarrow \mathrm{InCl} + \mathrm{e}^-$$

Interestingly, these interfacial degradation products may not be entirely detrimental. Over-extended cycling up to 500 cycles, they could potentially facilitate chloride-ion transport across the interface, partially alleviating capacity loss [54]. This nuanced behavior highlights the complex interplay between interfacial chemistry and electrochemical performance, meriting further investigation.

Moving forward, detailed phase-resolved studies probing both the bulk and interfacial regions are essential to fully elucidate the mechanisms governing structural transformation during cycling. Such insights will not only clarify the role of decomposition phases but also inspire strategies for optimizing stack pressure and particle engineering. Together, these findings open exciting opportunities for the rational design of next-generation chloride-ion battery materials, where controlled interfacial chemistry may become a key enabler of long-term performance.

2.4 | Mechanistic Comparison and Interfacial Kinetics

To place the all-solid-state VOCl/CSIC/In cell in the context of earlier VOCl chloride-ion batteries, Figure 5a compares the first-cycle galvanostatic profile of VOCl in a $PP_{14}Cl$–PC electrolyte (1M 1-butyl-1-methylpiperidinium chloride in propylene carbonate) with a Li anode [55] to the profile of the VOCl/CSIC/In full cell (Figure 5b). In the liquid cell, the smooth sloping charge–discharge curves between about 1.0 and 1.6 V vs. Li are consistent with the topochemical Cl^- intercalation/de-intercalation mechanism proposed by Gao et al., which involves partial intercalation of PP_{14}^+ species into the VOCl interlayers. In the solid-state configuration, where solvent and ionic liquid species are absent, and the anode is indium rather than lithium metal, the profile is instead centred around 0 V vs. In and exhibited a flatter plateau, in agreement with a direct conversion-type reaction pathway, corroborated by ex situ XRD showing the formation of VO-type phases upon discharge (Figure 4d). This comparison highlights that the transition from liquid to solid state primarily changes the operative reaction mechanism and polarization behaviour, while maintaining a comparable accessible capacity for VOCl (≈ 169–189 mAh g^{-1}). To place the performance of the optimized VOCl/CSIC/In cell in the context of state-of-the-art chloride-ion systems, we compile literature data for representative ASS-CIBs and related conversion-type solid-state batteries, including a well-established VOCl cell employing a liquid electrolyte, as summarized in Table 1.

All impedance measurements discussed in the following were performed on the solid-state cells only. To disentangle the individual interfacial contributions within the VOCl/CSIC/In architecture and monitor their evolution during operation, we carried out time-resolved EIS on symmetric cells (VOCl/CSIC/VOCl and In/CSIC/In) and on the full cell following the sequence of rest and cycling steps illustrated in Figure 5. The use of symmetric cells to isolate electrode–electrolyte interfaces is well established in impedance studies of batteries, and is particularly important for all-solid-state systems, where several processes with similar time constants frequently overlap in full-cell spectra [61]. For the VOCl/CSIC/VOCl symmetric cell, the Nyquist plots in Figure 5c show impedances in the kΩ range even in the fresh state, with a pronounced increase at mid to low frequency range during the 6 h rest period. This behaviour indicates that the VOCl–CSIC interface is intrinsically resistive and continues to evolve under open-circuit conditions, consistent with interphase growth and contact rearrangement at the cathode side [36]. In contrast, the In/CSIC/In symmetric cell (Figure 5d) remains in the Ω range over the same time window and exhibits only a modest increase in impedance, suggesting that the In/CSIC interface contributes a relatively small fraction of the total cell resistance under the present conditions. To better visualize and quantify the involved kinetic processes, model-independent DRT analysis was performed, which has been shown to provide deeper insight into interfacial and bulk contributions in all-solid-state batteries [62–64]. As shown in Figure S15a, the resistance contribution from the In/CSIC/In, especially that related to charge transfer, is about one order of magnitude lower than that from the VOCl/CSIC/VOCl during the time-resolved test. It is also observed in the DRT pattern that the characteristic time constant for different kinetic processes associated with the In anode and VOC cathode are closely spaced, a complete deconvolution of the full-cell during cycling would be difficult without further investigation of symmetric cells. However, the symmetric-cell data indicate the dominant, strongly time-dependent resistance in the VOCl/CSIC/In cell primarily to the cathode composite and its interface with CSIC, shown in Figure S15b.

Figure 5e,f illustrates the evolution of VOCl/CSIC/In full cell impedance, characterized by a continuous increase in impedance, from the fresh state through Cycle 10. The Nyquist plots are characterized by a barely distinguishable depressed semicircle in the mid-to-low frequency regime, which is typical of composite electrodes in all-solid-state batteries where charge transport through interphases and interfacial charge transfer occur on comparable time scales and cannot be easily separated into distinct RC features. The Warburg-like capacitive tail at low frequencies and its gradual increase with cycle number point to an increasing contribution from diffusion-controlled and porous-electrode-type processes rather than a single dominant interfacial resistance [65]. The Nyquist plots in Figure S12 (Cycles 0, 1, 2, and 10) illustrate this trend in more detail, showing a systematic increase in both the real and imaginary components of the impedance without the emergence of discrete semicircles.

A clearer evolution of resistance contribution is illustrated in their corresponding DRT pattern, as shown in Figure 6a. These different peaks on different time scales have been categorized based on typical kinetic processes in ASSBs, as suggested in the literature. The smaller peaks within the time regime τII between 10^{-5} and 10^{-2} s are indicative of charge transport across the as-formed interphase, and the more pronounced peaks observed in τIII regime between 10^{-2} and 100 s reflect charge-transfer processes of both electrodes. The individual contribution of impedance from the anode and cathode during cycling would require additional three-electrode cell experiments [64], which are beyond the scope of this study. However, the DRT pattern of the full-cell provides an insight into the overall cell impedance evolution of this system. After individually fitting these peaks, the corresponding changes in different resistances before and after cycling are presented in Figure 6b. It is shown that, in the VOCl/CSIC/In cell, changes in R_{ct} and R_{int} upon cycling are continuous and significant, and after 10 cycles, their values are almost 10 times higher than those observed in the pristine cell (cycle 0). This aligns well with the previous FIB-SEM and ex situ XRD analyses (Section 2.3), which revealed progressive particle cracking, void formation, and interfacial decomposition products within the VOCl/CSIC composite, suggesting a scenario in which the evolution of the VOCl–CSIC cathode interface and the tortuous transport pathways through the micrometre-sized VOCl particles can strongly influence the R_{ct} and R_{int}. These findings underline that further improvements in ASS-CIB performance will require coordinated optimization of interphase chemistry, VOCl particle size, and cathode composite architecture to suppress impedance growth.

3 | Conclusion

This study establishes a newly functional ASS-CIBs through the realization of a synergistic VOCl/$CsSn_{0.9}In_{0.067}Cl_3$ (CSIC)/In

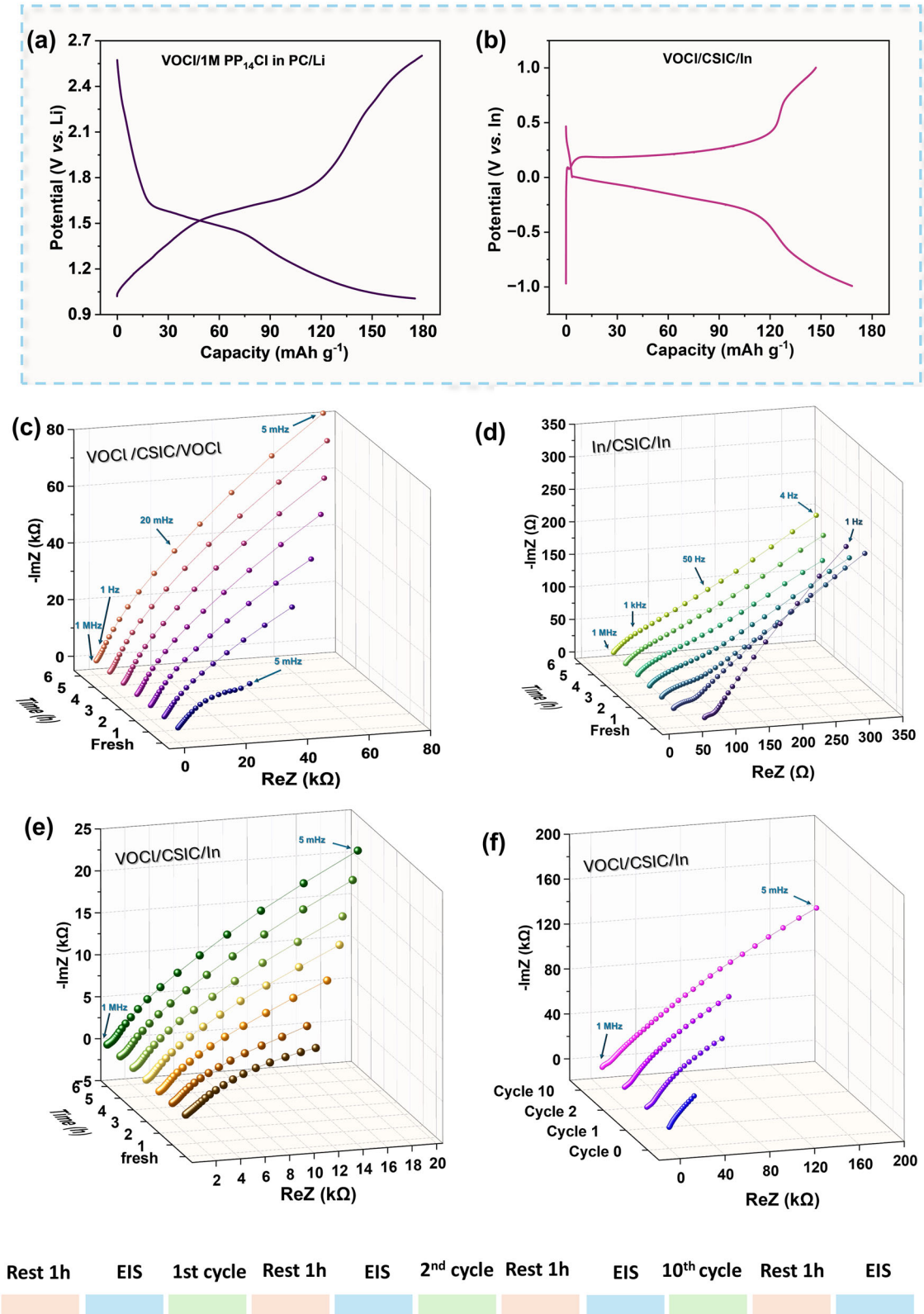

FIGURE 5 | Mechanistic comparison and impedance evolution of VOCl-cathode based chloride-ion cells: (a, b) first-cycle galvanostatic profiles for VOCl in $PP_{14}Cl$–PC/Li and in the all-solid-state VOCl/CSIC/In cell; (c–f) 3D Nyquist plots showing time- and cycle-dependent impedance evolution of VOCl/CSIC/VOCl and In/CSIC/In symmetric cells, and of the VOCl/CSIC/In full cell. The colored bars at the bottom illustrate the sequence of rest and EIS steps, where each EIS measurement was recorded after the corresponding galvanostatic cycling step.

TABLE 1 | Comparison of the VOCl/CSIC/In all solid-state cell with selected chloride ion and conversion type solid state batteries.

Cathode	Electrolyte	Anode	Initial discharge capacity (mAh g^{-1})	Number of cycles	Refs.
VOCl	$CsSn_{0.9}In_{0.067}Cl_3$ (Indium doped)	In	169	500	**This work**
VOCl	0.5 M $PP_{14}Cl$-PC (liquid electrolyte)	Li	189	100	[55]
$BiCl_3$	$CsSn_{0.95}Y_{0.05}Cl_{3.05}$ (Yttrium doped)	Sn	178	100	[56]
$WOCl_4$	$CsSn_{0.9}In_{0.067}Cl_3$ (Indium doped)	Li	108	20	[25]
AgCl	$CsSn_{0.925}Na_{0.075}Cl_{2.925}$ (Na doped)	Ag	64	30	[44]
AgCl	$CsSn_{0.925}Na_{0.075}Cl_{2.925}$ (Na doped)	Li-In	179	30	[44]
$MoCl_5$	$CsSn_{0.925}Na_{0.075}Cl_{2.925}$ (Na doped)	Li	135	1	[44]
$BiCl_3$	$Pb_{0.98}K_{0.02}Cl_{1.98}$ (K doped $PbCl_2$)	Pb	187	30	[57]
FeOCl	($[Al_{18}(\mu_2$-$OH)_{24}(OH_2)_{12}(mdip)_6]$ $6Cl{\cdot}6H_2O$) (cationic Al-based MOF)	Li	155	100	[58]
$BiCl_3$	$CsSn_{0.95}Y_{0.05}Cl_{3.05}$ (Yttrium doped)	Sn-carbon nanocomposite	188	15	[59]
$BiCl_3$	$CsSn_{0.95}Mn_{0.05}Cl_{3.05}$ (Manganese doped)	Sn	169	30	[60]

architecture. We showed that a 30:60:10 (VOCl:CSIC:C) cathode configuration represented a critical percolation threshold by methodically navigating the compositional space. This configuration optimizes ionic and electronic transport to achieve near-theoretical discharge capacities of 169 mAh g^{-1}. Our findings highlight the critical function of mechanical confinement, where customized stack pressures of up to 400 MPa act as a key lever to create close interfacial contact and encourage electrode densification, ultimately optimizing active site accessibility throughout the conversion process. Post-mortem analysis revealed the conversion-induced evolution through three complementary lenses: FIB-SEM imaging captured the microstructural reconfiguration, ex situ XRD tracked the emergence of cathode reaction products and interfacial side products, most notably CsCl and metallic Sn, and time-resolved EIS with DRT analysis shows that resistance growth is mainly associated with the VOCl–CSIC cathode interface, while the In–CSIC anode side remained comparatively stable. In particular, resistance contributions associated with interphase formation and charge-transfer processes increased progressively with cycling. We found that the formation of internal micro-voids and particle cracking, especially in the larger VOCl particle fractions, is closely related to the intrinsic structural breathing during cycling. This suggests that the polydispersity and average particle size are critical factors in the localized loss of interparticle connectivity. By delineating conversion chemistry from morphological stability, this study elucidates a mechanistic pathway for enhancing anionic shuttle battery performance. Going forward, controlled synthesis of sub-micron VOCl particles, deliberate regulation of interfacial reaction products, and DRT-assisted impedance diagnostics to pinpoint and reduce cathode-side resistance represent the most promising directions toward durable and high-performing ASS-anionic shuttle batteries.

4 | Experimental

4.1 | VOCl Synthesis

The precursor materials for the preparation of VOCl are VCl_3 (99+%, Sigma–Aldrich) and V_2O_3 (99.7%, Thermo Scientific); both materials react in a molar ratio 1:1.8 according to solid- gas transport reaction [55]

$$VCl_3 + V_2O_3 \rightarrow 3VOCl \quad (2)$$

A quartz ampoule measuring 180 mm in length and 20 mm in diameter was selected for loading the precursors. The composition comprised 850 mg of vanadium (III) chloride (VCl_3) and 450 mg of vanadium oxide (V_2O_3). The materials were hand-ground in a mortar for 15 min. Ampoules were sealed at a glass workshop in the presence of liquid nitrogen, maintaining

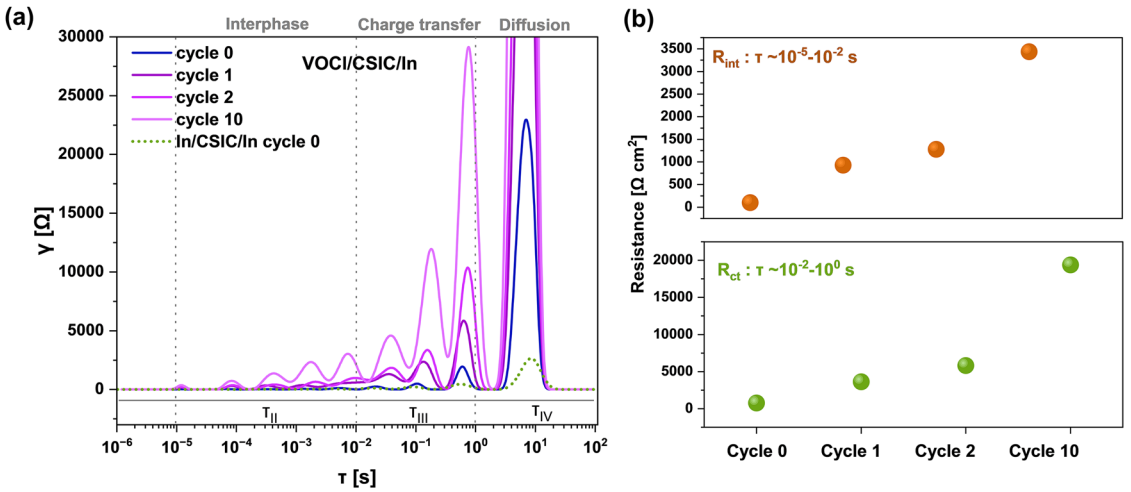

FIGURE 6 | EIS-DRT analysis of the VOCl/CSIC/In cells. (a) DRT pattern of cycled cells in Figure 5f and In symmetric cell after 5 h of rest (Figure 5d). The involved kinetic processes and their corresponding characteristic time constants are indicated. (b) Fitted resistances (interface and charge transfer) are categorized according to their characteristic time constants based on the literature in ASSBs.

a pressure of 2×10^{-3} mbar. Sealed ampoules were subjected to a controlled thermal regime in a muffle furnace (Carbolite Gero, CWF 1300), encompassing stepwise heating and cooling over 120 h at 893 K, with a ramp rate of 1 K min^{-1}. Upon removal from the furnace, the sealed ampoules revealed a dense, fine crystalline mass of purple-brown VOCl crystals. The ampoule was opened in a fume hood, and its contents were suspended in water to dissolve any unreacted compounds. The mixture was centrifuged (Hermle Labortechnik, Z 206 A) with water and acetone three times to separate the VOCl. The washed VOCl was stored in a vacuum oven (Thermo Fisher Scientific, VT 6060T) at 100°C overnight to dry.

4.2 | CSIC Synthesis

The electrolyte was synthesized utilizing a solid-state reaction via mechanochemical ball milling. The precursors CsCl (99.999%; Thermo Scientific), $SnCl_2$ (99.99%; Sigma–Aldrich), and $InCl_3$ (99.999%; Alfa Aesar) were preheated for 12 h (overnight) at a temperature of 120°C within a vacuum environment, supplemented by argon support, utilizing a glass oven (Büchi Corporation, B-585).

4.3 | Composite Electrode Preparation

All CAMs were prepared using a standardized mechanical ball-milling protocol. Four formulations—CAM 1 (55:15:30), CAM 2 (45:25:30), CAM 3 (30:60:10), and CAM 4 (20:50:30) by weight ratio of vanadium oxychloride (VOCl, 99.9%, Sigma–Aldrich), CSIC solid electrolyte, and Super P carbon (Alfa Aesar, 99+%), were synthesized to systematically investigate the influence of composition on electrochemical performance. For each composite, the cathode active material and half of the total carbon were first combined and loaded into the milling jar inside an argon-filled glovebox (O_2, H_2O < 0.1 ppm) to prevent any exposure to air or moisture. The sealed jar was then transferred out for milling at 250 rpm for 3 h in a planetary ball mill (Pulverisette 6, Fritsch, Germany). After milling, the jar was returned to the glovebox and opened only under an argon atmosphere. The solid electrolyte and the remaining carbon were then added inside the glovebox, and the jar was resealed and subjected to a second identical milling step. Finally, all powders were collected and homogenized by a further hour of milling, with all handling and transfers performed exclusively under argon to eliminate any risk of reactivity or contamination. For comparative studies involving reduced VOCl particle size, the pristine VOCl powder was first subjected to high-energy ball-milling at 600 rpm for 2 h.

The Indium-based anode composite was prepared by thoroughly mixing Indium mesh powder (40 wt.%, 99.99%, 100 mesh, Thermo Scientific), CSIC solid electrolyte (50 wt.%), and dried carbon black (10 wt.%, Alfa Aesar, 99+%) in a stoichiometric ratio, followed by hand grinding in an agate mortar for 15 min inside the glovebox to ensure uniformity and to maintain an inert environment throughout the process.

4.4 | Cell Assembly and Electrochemical Measurements

ASS-CIBs were assembled entirely in an argon-filled glovebox (O_2, H_2O < 0.1 ppm) to prevent exposure to air and moisture. For each cell, 80 mg of CSIC solid electrolyte, 5 mg of cathode composite, and 4 mg of indium-based anode composite were sequentially layered inside the internal sleeve of the solid-state test cell (8 mm diameter), with each layer compacted using a calibrated torque wrench for 3 min to ensure optimal densification and interfacial contact. Galvanostatic charge–discharge and CV measurements were conducted at 60°C using a Biologic MPG2 multi-channel Potentiostat at various current densities. Before testing, cells were aged for 6 h to ensure interfacial equilibration. All electrochemical measurements, including cycling and impedance spectroscopy, were performed within the temperature-controlled climate chamber to maintain fixed temperature conditions. Ionic conductivity measurements of CSIC were carried out using a Biologic SP-150e single-channel Potentiostat.

4.5 | X-Ray Diffraction

XRD was utilized to investigate the diffraction patterns of the synthesized cathode, electrolyte, composite powders, and the phase changes in the active material and anode after galvanostatic discharge. The measurements were conducted with a STOE STADI-P diffractometer (operated at 50 kV, 40 mA) in Debye-Scherrer geometry, using Mo $K_{\alpha 1}$ radiation ($\lambda = 0.7093$ Å). Data acquisition was performed over an angular range of $2\theta = 2°$ to 50°, with a total measurement duration of 30 min and a step size of 4.5°. The data were analysed using Rietveld refinement with TOPAS (Bruker AXS, Version 5) software. The distribution of instrumental intensity was established based on a reference scan of LaB_6. All thermal factors remained constant for the Rietveld analysis.

4.6 | Scanning Electron Microscope

All the CAMs were pelletized within an 8 mm solid-state cell for overnight at a pressure of 250 MPa to mimic the surface topology of the cathode composite in its pristine state. Surface morphology of the CAM, SE, and composite cathode pellets was characterized using a Thermo Scientific Apreo 2 FESEM. Imaging was performed at an accelerating voltage of 5 kV and a beam current of 1.6 nA. Elemental mapping was conducted at 20 kV and 6.4 nA with a dwell time of 10 min.

4.7 | Focussed Ion Beam- Scanning Electron Microscopy (FIB-SEM)

The cross-section images of the pristine and cycled cathode pellets were captured using the Zeiss NVision 40 FIB-SEM. The Ga^+ FIB was used to mill the composite cathode. The images were captured with tilt correction enabled, utilizing a stage tilt of 54° and a tilt angle of 36° between the electron beam and the cross-section. The images were captured with 5 kV using the Everhart-Thornley detector and Inlens secondary electron detector, respectively. Semi-quantitative pore analysis was performed on representative FIB-SEM images. Images acquired at different magnifications were first cropped to a common magnification, after which the pore phase was segmented using the Labkit plugin in Fiji and quantified by area measurement using the Measure function.

4.8 | Particle Size Analysis

Particle size distribution of the VOCl powder was measured by laser diffraction using a Malvern Panalytical Mastersizer instrument. Volume-weighted size distributions are reported as D_{10}, D_{50}, and D_{90} values.

Author Contributions

Anantha Padmanabhan Gopikuttan: investigation, Writing – original draft, methodology, visualization, Writing – review and editing, formal analysis, data curation. **Soutam Panja**: conceptualization, investigation, writing – original draft, methodology, visualization, writing – review and editing, software, project administration, data curation. **Manuel Mundszinger**: methodology, data curation, formal analysis. **Amr Radwan**: visualization, validation, methodology. **Johannes Biskupek**: writing – review and editing, project administration, formal analysis. **Hong Chen**: investigation, formal analysis. **Maximilian Fichtner**: conceptualization, funding acquisition, writing – review and editing, visualization, resources, supervision, project administration, formal analysis, validation, data curation, methodology. **Oliver Clemens**: writing – review and editing, validation, formal analysis, supervision, data curation.

Acknowledgements

The authors gratefully acknowledge financial support from the Deutsche Forschungsgemeinschaft (DFG, German Research Foundation) under Germany's Excellence Strategy – EXC 2154 – Project ID 390874152 (POLiS Cluster of Excellence). Additionally, S.P. expresses gratitude to Guruprakash Karkera and Mervyn Soans for their valuable assistance with the CSIC solid electrolytes. This work contributes to the research performed at CELEST (Centre for Electrochemical Energy Storage Ulm-Karlsruhe).

Open access funding enabled and organized by Projekt DEAL.

Conflicts of Interest

The authors declare no conflicts of interest.

Data Availability Statement

To ensure transparency, all data associated with this research (both raw and processed measurements) was managed using Kadi4mat, the Karlsruhe data infrastructure for materials science. This adheres to the FAIR principles (Findable, Accessible, Interoperable, and Reusable) as recommended by the German Research Foundation. The data is publicly available through the Zenodo open repository with the following DOI for easy access: https://doi.org/10.5281/zenodo.18710799.

References

1. R. Yokoi, R. Kataoka, T. Masese, et al., "Potentials and Hotspots of Post-Lithium-Ion Batteries: Environmental Impacts and Supply Risks for Sodium- and Potassium-Ion Batteries," *Resources, Conservation and Recycling* 204 (2024): 107526, https://doi.org/10.1016/j.resconrec.2024.107526.

2. K. M. Abraham, "How Comparable Are Sodium-Ion Batteries to Lithium-Ion Counterparts?," *ACS Energy Letters* 5 (2020): 3544–3547, https://doi.org/10.1021/acsenergylett.0c02181.

3. Y. Liang, H. Dong, D. Aurbach, and Y. Yao, "Current Status and Future Directions of Multivalent Metal-Ion Batteries," *Nature Energy* 5 (2020): 646–656, https://doi.org/10.1038/s41560-020-0655-0.

4. J. Wu, Q. Yang, J. Li, et al., "Origin of Storage Capacity Enhancement by Replacing Univalent Ion With Multivalent Ion for Energy Storage," *Electrochimica Acta* 282 (2018): 30–37, https://doi.org/10.1016/j.electacta.2018.06.032.

5. M. R. Palacin, P. Johansson, R. Dominko, et al., "Roadmap on Multivalent Batteries," *Journal of Physics: Energy* 6 (2024): 031501.

6. F. Gschwind, H. Euchner, and G. Rodriguez-Garcia, "Chloride Ion Battery Review: Theoretical Calculations, State of the Art, Safety, Toxicity, and an Outlook towards Future Developments," *European Journal of Inorganic Chemistry* 2017 (2017): 2784–2799, https://doi.org/10.1002/ejic.201700288.

7. T. Liu, N. Peng, X. Zhang, et al., "Insight Into Anion Storage Batteries: Materials, Properties and Challenges," *Energy Storage Materials* 42 (2021): 42–67, https://doi.org/10.1016/j.ensm.2021.07.011.

8. M. Anji Reddy and M. Fichtner, "Batteries Based on Fluoride Shuttle," *Journal of Materials Chemistry* 21 (2011): 17059, https://doi.org/10.1039/c1jm13535j.

9. C. Zhang, "Batteries: Shuttling chloride ions," *Nature Energy* 1 (2016): 16047.

10. Q. Liu, Y. Wang, X. Yang, et al., "Rechargeable Anion-Shuttle Batteries for Low-Cost Energy Storage," *Chem* 7 (2021): 1993–2021.

11. S. Panja, Y. Miao, J. Döhn, et al., "Synthesis, Structural Analysis, and Degradation Behavior of Potassium Tin Chloride as Chloride-Ion Batteries Conversion Electrode Material," *Advanced Functional Materials* 35 (2024): 2413489.

12. X. Zhao, Z. Zhao-Karger, D. Wang, and M. Fichtner, "Metal Oxychlorides as Cathode Materials for Chloride Ion Batteries," *Angewandte Chemie International Edition* 52 (2013): 13621–13624, https://doi.org/10.1002/anie.201307314.

13. S. Kalnaus, N. J. Dudney, A. S. Westover, E. Herbert, and S. Hackney, "Solid-State Batteries: The Critical Role of Mechanics," *Science* 381 (2023): abg5998.

14. Y. Xiao, Y. Wang, S. H. Bo, J. C. Kim, L. J. Miara, and G. Ceder, "Understanding Interface Stability in Solid-State Batteries," *Nature Research* 5 (2020): 105–126.

15. F. Han, A. S. Westover, J. Yue, et al., "High Electronic Conductivity as the Origin of Lithium Dendrite Formation Within Solid Electrolytes," *Nature Energy* 4 (2019): 187–196, https://doi.org/10.1038/s41560-018-0312-z.

16. B. Hao, W. Chen, J. Wu, Z. J. Jiang, X. Chen, and Z. Jiang, "Long-Term Cycling Stability and Dendrite Suppression in Garnet-Type Solid-State Lithium Batteries via Plasma-Induced Artificial SEI Layer Formation," *Advanced Functional Materials* 35 (2025): 2502429.

17. K. Yoon, H. Kim, S. Han, et al., "Detrimental Effect of High-Temperature Storage on Sulfide-Based All-Solid-State Batteries," *Applied Physics Reviews* 9 (2022): 031403.

18. S. Narayanan, U. Ulissi, J. S. Gibson, Y. A. Chart, R. S. Weatherup, and M. Pasta, "Effect of Current Density on the Solid Electrolyte Interphase Formation at the lithium|Li_6PS_5Cl Interface," *Nature Communications* 13 (2022): 7237.

19. C. Lee, J. Y. Kim, K. Y. Bae, et al., "Enhancing Electrochemomechanics: How Stack Pressure Regulation Affects All-Solid-State Batteries," *Energy Storage Materials* 66 (2024): 103196.

20. P. Gao, C. Wall, L. Zhang, M. A. Reddy, and M. Fichtner, "Vanadium Oxychloride as Electrode Material for Sodium Ion Batteries," *Electrochemistry Communications* 60 (2015): 180–184, https://doi.org/10.1016/j.elecom.2015.09.008.

21. K. P. Lakshmi, K. J. Janas, and M. M. Shaijumon, "Antimony Oxychloride Embedded Graphene Nanocomposite as Efficient Cathode Material for Chloride Ion Batteries," *Journal of Power Sources* 433 (2019): 126685.

22. P. Gao, X. Zhao, Z. Zhao-Karger, T. Diemant, R. J. Behm, and M. Fichtner, "Vanadium Oxychloride/Magnesium Electrode Systems for Chloride Ion Batteries," *ACS Applied Materials & Interfaces* 6 (2014): 22430–22435, https://doi.org/10.1021/am5064266.

23. J. P. Vénien, P. Palvadeau, D. Schleich, and J. Rouxel, "Vanadium (III) oxychloride: Magnetic, Optical and Electrical Properties; Lithium and Molecular Intercalations," *Materials Research Bulletin* 14 (1979): 891.

24. L. Xu, Y. H. Xiong, J. W. Meng, et al., "Redox behavior of indium in molten chlorides," *Transactions of Nonferrous Metals Society of China (English Edition)* 31 (2021): 1496–1505.

25. G. Karkera, M. Soans, A. Akbaş, et al., "A Structurally Flexible Halide Solid Electrolyte with High Ionic Conductivity and Air Processability," *Advanced Energy Materials* 13 (2023): 2300982.

26. Y. Yamamoto, Y. Iriyama, and S. Muto, "Analysis of Void Volume in Composite Electrode of All-solid-state Lithium-ion Battery Employing FIB-SEM and Union Operation Image Processing," *Microscopy and Microanalysis* 23 (2017): 314–315, https://doi.org/10.1017/S1431927617002252.

27. Z. Ding, Y. Tang, V. Sai, et al., "Exploring the influence of focused ion beam processing and scanning electron microscopy imaging on solid-state electrolytes," *Microscopy* 72, 4 (2023): 326–335, https://doi.org/10.1093/jmicro/dfac064.

28. K. S. Saqib, T. J. Embleton, J. H. Choi, et al., "Correction to "Understanding the Carbon Additive/Sulfide Solid Electrolyte Interface in Nickel-Rich Cathode Composites and Prioritizing the Corresponding Interplay Between the Electrical and Ionic Conductive Networks to Enhance All-Solid-State-Battery Rate Capability"," *ACS Applied Materials & Interfaces* 17 (2025): 26090, https://doi.org/10.1021/acsami.5c04614.

29. S. Yanev, C. Heubner, K. Nikolowski, M. Partsch, H. Auer, and A. Michaelis, "Editors' Choice—Alleviating the Kinetic Limitations of the Li-In Alloy Anode in All-Solid-State Batteries," *Journal of The Electrochemical Society* 171 (2024): 020512, https://doi.org/10.1149/1945-7111/ad2594.

30. T. Shi, Q. Tu, Y. Tian, et al., "High Active Material Loading in All-Solid-State Battery Electrode via Particle Size Optimization," *Advanced Energy Materials* 10 (2020): 1902881.

31. X. Han, Y. Xu, H. Li, et al., "Mechanically Robust Halide Electrolytes for High-Performance All-Solid-State Batteries," *Nature Communications* 16 (2025): 9770, https://doi.org/10.1038/s41467-025-64726-y.

32. J. A. Lewis, J. Tippens, F. J. Q. Cortes, and M. T. McDowell, "Chemo-Mechanical Challenges in Solid-State Batteries," *Trends in Chemistry* 1 (2019): 845–857, https://doi.org/10.1016/j.trechm.2019.06.013.

33. J.-M. Doux, Y. Yang, D. H. S. Tan, et al., "Pressure Effects on Sulfide Electrolytes for All Solid-State Batteries," *Journal of Materials Chemistry A* 8 (2020): 5049–5055, https://doi.org/10.1039/C9TA12889A.

34. S. S. Shin, J.-S. Kim, S. Choi, et al., "Quantitative Determination of Lithium Depletion During Rapid Cycling in Sulfide-Based All-Solid-State Batteries," *Chemical Communications* 57 (2021): 3453–3456, https://doi.org/10.1039/D0CC08367D.

35. C.-Y. Yu, J. Choi, J. Dunham, et al., "Time-Resolved Impedance Spectroscopy Analysis of Aging in Sulfide-Based All-Solid-State Battery Full-Cells Using Distribution of Relaxation Times Technique," *Journal of Power Sources* 597 (2024): 234116, https://doi.org/10.1016/j.jpowsour.2024.234116.

36. P. Vadhva, J. Hu, M. J. Johnson, et al., "Electrochemical Impedance Spectroscopy for All-Solid-State Batteries: Theory, Methods and Future Outlook," *ChemElectroChem* 8 (2021): 1930–1947, https://doi.org/10.1002/celc.202100108.

37. B. Liu, S. D. Pu, C. Doerrer, et al., "The Effect of Volume Change and Stack Pressure on Solid-State Battery Cathodes," *SusMat* 3 (2023): 721.

38. W. Zhang, D. A. Weber, H. Weigand, et al., "Interfacial Processes and Influence of Composite Cathode Microstructure Controlling the Performance of All-Solid-State Lithium Batteries," *ACS Applied Materials & Interfaces* 9 (2017): 17835–17845, https://doi.org/10.1021/acsami.7b01137.

39. M. Amirabbasi and M. Ekholm, "Lattice Distortions and Magnetic Interactions in Single-Layer VOCl," *Physical Review Materials* 7 (2023): 074003.

40. C. Liu, F. Roters, and D. Raabe, "Author Correction: Acceleration of Radiative Recombination for Efficient Perovskite LEDs," *Nature* 630 (2024): E15, https://doi.org/10.1038/s41586-024-07665-w.

41. L. L. Driscoll, E. H. Driscoll, B. Dong, et al., "Under Pressure: Offering Fundamental Insight Into Structural Changes on Ball Milling Battery Materials," *Energy & Environmental Science* 16 (2023): 5196–5209, https://doi.org/10.1039/D3EE00249G.

42. T. Pajkossy, "Analysis of Quasi-Reversible Cyclic Voltammograms: Transformation to Scan-Rate Independent Form," *Electrochemistry Communications* 90 (2018): 69–72, https://doi.org/10.1016/j.elecom.2018.04.004.

43. T. Kim, W. Choi, H. C. Shin, et al., "Applications of Voltammetry in Lithium Ion Battery Research," *Journal of Electrochemical Science and Technology* 11 (2020): 14–25.

44. T. Xia, Q. Li, Z. Xue, Y. Miao, X. Shen, and X. Zhao, "Boosting the Structural and Electrochemical Stability of Chloride-Ion-Conducting Perovskite Solid Electrolytes by Alkali Ion Doping," *Advanced Materials* 37 (2024): 2411605.

45. F. Wu and G. Yushin, "Conversion Cathodes for Rechargeable Lithium and Lithium-Ion Batteries," *Energy & Environmental Science* 10 (2017): 435–459.

46. A. K. Padhi, K. S. Nanjundaswamy, and J. B. Goodenough, "Phospho-olivines as Positive-Electrode Materials for Rechargeable Lithium Batteries," *Journal of The Electrochemical Society* 144 4 (1997): 1188, https://doi.org/10.1149/1.1837571.

47. M. S. Whittingham, "Lithium Batteries and Cathode Materials," *Chemical Reviews* 104 (2004): 4271–4302, https://doi.org/10.1021/cr020731c.

48. Y. Ali, N. Iqbal, and S. Lee, "Simultaneous Effect of Particle Size and Location on Stress Development in the Electrodes of Lithium-Ion Batteries," *International Journal of Energy Research* 44 (2020): 12145–12157, https://doi.org/10.1002/er.5795.

49. L. Wheatcroft, A. Bird, J. C. Stallard, et al., "Fracture Testing of Lithium-Ion Battery Cathode Secondary Particles in-situ inside the Scanning Electron Microscope," *Batteries & Supercaps* 6 (2023): 202300032.

50. P. Bleith, H. Kaiser, P. Novák, and C. Villevieille, "In Situ X-Ray Diffraction Characterisation of $Fe_{0.5}TiOPO_4$ and $Cu_{0.5}TiOPO_4$ as Electrode Material for Sodium-Ion Batteries," *Electrochimica Acta* 176 (2015): 18–21, https://doi.org/10.1016/j.electacta.2015.06.105.

51. Z. Huang, H. Gao, Z. Yang, et al., "Improved Capacity and Cycling Stability of SnO_2 Nanoanode Induced by Amorphization During Cycling for Lithium Ion Batteries," *Materials and Design* 180 (2019): 107973.

52. X. Zhao, Q. Li, T. Yu, M. Yang, K. Fink, and X. Shen, "Carbon Incorporation Effects and Reaction Mechanism of FeOCl Cathode Materials for Chloride Ion Batteries," *Scientific Reports* 6 (2016): 19448.

53. P. Naillou, A. Boulineau, E. De Vito, E. Lavanant, and P. Azaïs, "Direct Observation of Li_6PS_5Cl–NMC Electrochemical Reactivity in All-Solid-State Cells," *Energy Storage Materials* 75 (2025): 104050.

54. W. D. Richards, L. J. Miara, Y. Wang, J. C. Kim, and G. Ceder, "Interface Stability in Solid-State Batteries," *Chemistry of Materials* 28 (2016): 266–273, https://doi.org/10.1021/acs.chemmater.5b04082.

55. P. Gao, M. A. Reddy, X. Mu, et al., "VOCl as a Cathode for Rechargeable Chloride Ion Batteries," *Angewandte Chemie* 128 (2016): 4357–4362, https://doi.org/10.1002/ange.201509564.

56. L. Zhao, A. Inoishi, H. Miki, et al., "Super Chloride Ionic Conductivity in $CsSnCl_3$-Based Perovskite Compound and Its Application for Solid-State Chloride Batteries," *Advanced Energy and Sustainability Research* 5 (2024): 2400198.

57. R. Sakamoto, N. Shirai, A. Inoishi, and S. Okada, "All-Solid-State Chloride-Ion Battery With Inorganic Solid Electrolyte," *ChemElectroChem* 8 (2021): 4441–4444, https://doi.org/10.1002/celc.202101017.

58. V. G. Martello, A. Piovano, M. Bonomo, M. Dincă, S. Bordiga, and C. Gerbaldi, "A Leap Toward Quasi-Solid-State Chloride-Ion Batteries With Metal–Organic Frameworks," *ACS Energy Letters* 11 (2026): 419–425, https://doi.org/10.1021/acsenergylett.5c02431.

59. H. Yang, S. Kim, S. Lee, et al., "Sn–Carbon Nanocomposite Anode for All-Solid-State Chloride-Ion Batteries Operating at Room Temperature," *Chemical Communications* 61 (2025): 1866–1869, https://doi.org/10.1039/D4CC05595K.

60. R. Sakamoto, N. Shirai, L. Zhao, A. Inoishi, H. Sakaebe, and S. Okada, "Room-temperature Operation of All-solid-state Chloride-ion Battery with Perovskite-type $CsSn_{0.95}Mn_{0.05}Cl_3$ as a Solid Electrolyte," *Electrochemistry* 91 (2023): 077003.

61. G. Portalis, E. Carrapa, B. Simon, and V. Vivier, "Electrochemical Impedance Spectroscopy Investigation on Battery Materials Using a Symmetrical Cell," *Journal of Solid State Electrochemistry* 25 (2021): 1915–1926, https://doi.org/10.1007/s10008-021-04962-6.

62. H. Chen, P. Bal, and O. Clemens, "Complex Influence of Stack Pressure on BiF_3 Cathode Materials in All-Solid-State Fluoride-Ion Batteries," *Journal of Materials Chemistry A* 14 (2026): 3318–3330, https://doi.org/10.1039/D5TA06611E.

63. Y. Lu, C.-Z. Zhao, J.-Q. Huang, and Q. Zhang, "The Timescale Identification Decoupling Complicated Kinetic Processes in Lithium Batteries," *Joule* 6 (2022): 1172–1198, https://doi.org/10.1016/j.joule.2022.05.005.

64. R. Zhang, A. Kondrakov, J. Janek, and T. Brezesinski, "Timescale Identification of Electrochemical Processes in All-Solid-State Batteries Using an Advanced Three-Electrode Cell Setup," *Energy Storage Materials* 75 (2025): 104000, https://doi.org/10.1016/j.ensm.2025.104000.

65. M. Gerle, N. Wagner, J. Häcker, M. Nojabaee, and K. A. Friedrich, "Identification of the Underlying Processes in Impedance Response of Sulfur/Carbon Composite Cathodes at Different SOC," *Journal of The Electrochemical Society* 169 (2022): 030505, https://doi.org/10.1149/1945-7111/ac56a4.

Supporting Information

Additional supporting information can be found online in the Supporting Information section.

Supporting File: aenm71335-sup-0001-SuppMat.docx.